Volume 14
Number 27
21 July 2022
Pages 9529-9934

# Nanoscale

rsc.li/nanoscale

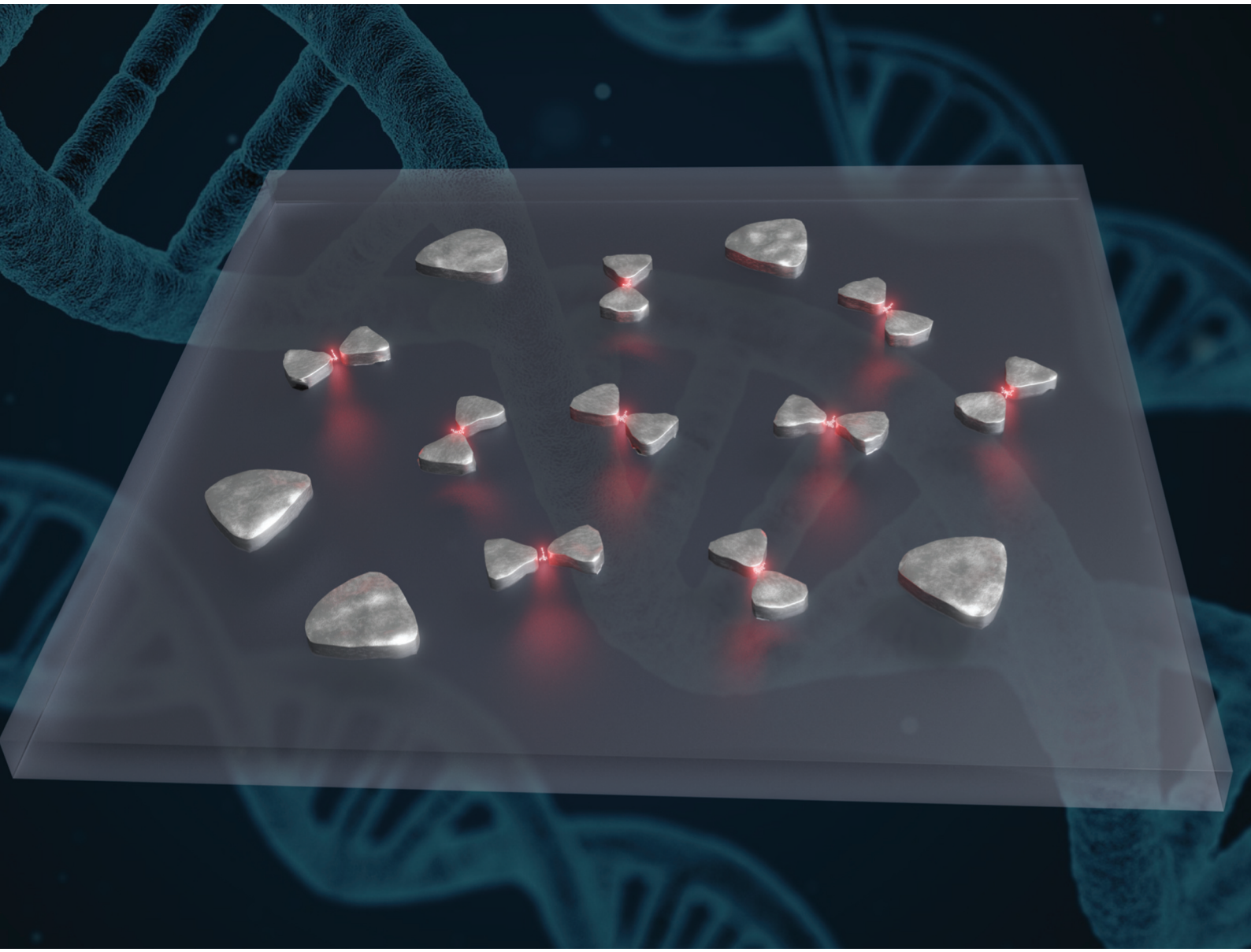

ISSN 2040-3372

ROYAL SOCIETY OF CHEMISTRY

**COMMUNICATION**
Tommi K. Hakala, Veikko Linko *et al.*
Optical characterization of DNA origami-shaped silver nanoparticles created through biotemplated lithography

NCNST

Nanoscale

ROYAL SOCIETY OF CHEMISTRY

COMMUNICATION

View Article Online
View Journal | View Issue



Cite this: *Nanoscale*, 2022, **14**, 9648

Received 22nd September 2021,
Accepted 12th June 2022

DOI: 10.1039/d1nr06256e

rsc.li/nanoscale

# Optical characterization of DNA origami-shaped silver nanoparticles created through biotemplated lithography†

Kabusure M. Kabusure, ‡[a] Petteri Piskunen, ‡[b] Jiaqi Yang,[a] Mikko Kataja,[a] Mwita Chacha,[a] Sofia Ojasalo,[b] Boxuan Shen,[b,c] Tommi K. Hakala *[a] and Veikko Linko *[b,d]

**Here, we study optically resonant substrates fabricated using the previously reported BLIN (biotemplated lithography of inorganic nanostructures) technique with single triangle and bowtie DNA origami as templates. We present the first optical characterization of BLIN-fabricated origami-shaped silver nanoparticle patterns on glass surfaces, comprising optical transmission measurements and surface-enhanced Raman spectroscopy. The formed nanoparticle patterns are examined by optical transmission measurements and used for surface enhanced Raman spectroscopy (SERS) of Rhodamine 6G (R6G) dye molecules. Polarization-resolved simulations reveal that the higher SERS enhancement observed for the bowties is primarily due to spectral overlap of the optical resonances with the Raman transitions of R6G. The results manifest the applicability of the BLIN method and substantiate its potential in parallel and high-throughput substrate manufacturing with engineered optical properties. While the results demonstrate the crucial role of the formed nanogaps for SERS, the DNA origami may enable even more complex nanopatterns for various optical applications.**



## 1. Introduction

Plasmonic nanostructures have gained their popularity in different research areas such as photovoltaics,[1,2] biosensing,[3] and molecular imaging[4] due to their unique properties of manipulating light at nanoscale. Besides the commonly employed direct lithographic writing[5] and wet chemistry methods,[6] there also exist multiple routes to achieve user-defined plasmonic nanostructures through molecular self-assembly. One of them is structural DNA nanotechnology[7–9] that has found a plethora of implementations in *e.g.* biomedicine,[10,11] bioengineering,[12] nanoelectronics[13] and robotics,[14,15] but which may be equally used for high-throughput spatial arrangement of various components for nano photonic and materials science applications.[16,17] Arguably, the most common technique to form DNA-based templates is the versatile and robust DNA origami method[18–21] that enables outstanding addressability and precision. Although DNA itself is not electrically conductive nor optically very intriguing, there is a great deal of studies that have manifested the feasibility of DNA origami as high-resolution "pegboards" for directing the programmable assembly of nanocomponents *e.g.* conductive polymers,[22,23] carbon nanotubes,[24,25] fluorescent dyes,[26,27] plasmonic nanoparticles,[28–34] and superlattice-forming particles.[35–38]

Yet, there exist other possibilities to harness the spatial accuracy of DNA nanostructures in nanofabrication[39–42] to form optically resonant materials.[43–45] These include discrete DNA origami molds for casting metal and plasmonic nanoparticles with predefined dimensions in solution phase[46–48] and a combination of bottom-up-based DNA origami and common top-down lithography methods for surface-assisted nanopatterning. The latter can be achieved either by precision placement[49,50] of fluorescently labeled DNA structures into engineered nanoarrays,[51,52] or by using DNA origami as a lithographic mask to pattern DNA origami-shaped metal nanoparticles on a substrate.[53–55]

Here, we use our very recently developed biotemplated lithography of inorganic nanostructures (BLIN) technique[56] to decorate transparent surfaces with metal nanoparticles and characterize them by optical means. Unlike the previously introduced DNA-assisted lithography (DALI),[54] which is highly selective to some key materials (*e.g.* Al, Ti, Ag, to mention a few) determined by a hydrofluoric acid etching process, BLIN allows the use of in-

[a]*Department of Physics and Mathematics, University of Eastern Finland, Yliopistokatu 2, P.O Box 111, FI-80101 Joensuu, Finland. E-mail: tommi.hakala@uef.fi*
[b]*Biohybrid Materials, Department of Bioproducts and Biosystems, Aalto University, P.O. Box 16100, FI-00076 Aalto, Finland. E-mail: veikko.linko@aalto.fi*
[c]*Department of Medical Biochemistry and Biophysics, Karolinska Institutet, 17165 Stockholm, Sweden*
[d]*LIBER Center of Excellence, Aalto University, P.O. Box 16100, FI-00076 Aalto, Finland*

†Electronic supplementary information (ESI) available: AFM images of DNA templates, additional SEM images of particles, particle coverage of the substrates, and simulated absorption and scattering spectra of the particles. See DOI: https://doi.org/10.1039/d1nr06256e

‡These authors contributed equally to this work.

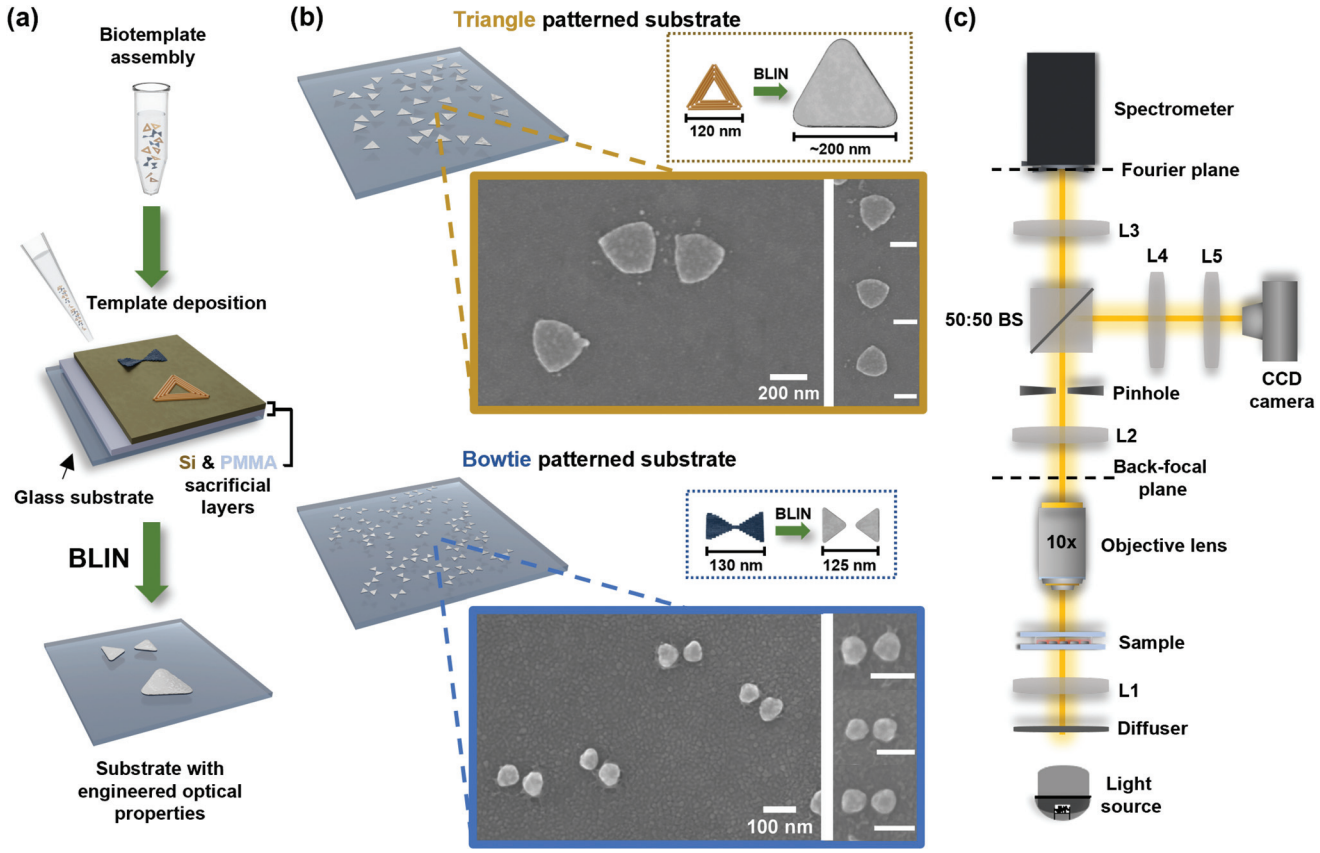


**Fig. 1** Fabrication of optically resonant substrates. (a) Folded DNA origami templates (bowties and triangles, see Fig. S1 in the ESI† for AFM images) are deposited on a glass substrate (1.1 μm thickness) coated with a sacrificial layer of poly(methyl methacrylate) (PMMA) (40 nm) topped with silicon (100 nm). The BLIN technique allows transferring the shape of DNA origami to silver nanostructures. (b) SEM images of the ready optically resonant substrates and close-up images of the individual structures. The target structures cover ~1% of the patterned surface areas (see ESI†). The scale bars in the close-up images are 200 nm and 100 nm for triangles and bowties, respectively. The insets schematically show how the spatial information of a DNA origami template is transferred during the BLIN processing. (c) Experimental setup for the far-field transmission measurements. Unpolarized white light goes through the diffuser before it hits the sample. The 10× objective lens focuses the incoming light to the 50 : 50 beam splitter. Finally, the light is simultaneously detected by both the CCD camera and the spectrometer.

expensive transparent substrates such as silica-based glass for optical applications. We combine the BLIN fabrication scheme with triangle[18] and bowtie[54] DNA origami templates (Fig. 1a) and form billions of origami-shape silver nanoparticles on ~1 $cm^2$ glass substrates in a parallel fashion (Fig. 1b).

We show that bowtie-shaped silver nanoparticle surfaces may act as optically resonant substrates for Raman-enhanced spectroscopy (SERS) and transmission-based characterization. We demonstrate experimentally that by depositing Rhodamine 6G (R6G) molecules onto the BLIN-fabricated substrates, bowties produce more prominent Raman signal enhancement than the single triangles. To further support this observation, we perform finite difference time domain (FDTD) simulations for both single triangles and bowties. We present the simulations of the far-field and near-field distributions of both single triangles and bowties at different polarizations.

The near-field distributions show that bowties exhibit higher field enhancements as compared to the single triangles with the longitudinal polarization. For the transverse polarization, single triangles and bowties exhibit relatively similar field enhancements. By further optimization, we expect to achieve even smaller structures and nanosized gaps. Such structures could exhibit even higher plasmonic near field enhancements that are crucial in various applications, for instance in SERS-based biosensing, as well as in plasmonics with resonances at the visible and near infrared wavelengths.

## 2. Methods

### 2.1. DNA origami fabrication and deposition

The design protocol and the staple strand sequences for bowtie and triangle DNA origami structures have been described in their original publications.[18,54] The folding solution was prepared by mixing ~10× excess of staple strands (purchased from IDT) with 20 nM of 7249 nt long M13mp18 scaffold strand (purchased from Tilibit Nanosystems) in folding buffer (FOB) composed of 1× TAE buffer (40 mM Tris,

19 mM acetic acid, 1 mM ethylenediaminetetraacetic acid (EDTA)) and 12.5 mM $Mg^{2+}$ at pH ~8.3. The structures were subsequently folded according to the original protocols[18,54] (Fig. 1a). The quality of DNA origami folding was verified using atomic force microscopy (AFM) (see Fig. S1 in the ESI†).

The ready origami structures were diluted to 5 nM concentration in $Mg^{2+}$ supplemented TAE (1× TAE buffer with 100 mM $Mg^{2+}$) and then a 10 μl droplet was deposited on a 10 × 10 $cm^2$ indium tin oxide (ITO) glass chip coated with silicon and PMMA layers (Fig. 1a). The ITO glass substrate was chosen since it is electrically conductive and thus applying further conductive coatings later was not necessary for electron microscopy imaging. Prior to the origami deposition, a negative surface charge was generated on the chip with an oxygen plasma treatment in an Oxford Instruments Plasmalab 80 Plus reactive ion etching tool (duration: 120 s, gas flow: $O_2$ 45 sccm and Ar 5 sccm, process pressure: 250 mTorr, RF power: 50 W). Following deposition, the origami were incubated for 5 min at room temperature and then rinsed 3× with 100 μL of $ddH_2O$. After rinsing, the chips were dried under a $N_2$ flow. The 5 nM DNA origami concentration was chosen to yield a final metal particle coverage (see 2.2) dense enough to produce detectable ensemble averaged effects as the measurements are from a large area rather than from individual nanostructures. On the other hand, the density was chosen to be low enough to avoid fabrication mask collapse[56] due to overpopulation.

### 2.2. Biotemplated lithography and imaging

After the origami were deposited on the chips, BLIN was employed to fabricate nanostructures based on the templates. The BLIN fabrication method and all materials used for the process are described in detail previously.[56] The core steps in the process consist of (1) a selective silicon oxide growth where the biotemplates locally inhibit the growth of a silicon oxide layer, thus transferring their shape into the masking layer,[57] (2) conventional nanofabrication techniques (reactive ion etching (RIE) and physical vapor deposition (PVD)) that create nanostructures based on the masking layer and finally, (3) a solvent lift-off step that removes all processing layers from the substrate.

To facilitate the lift-off, a 40 nm sacrificial layer of A1 poly (methyl methacrylate) (PMMA) (A1: 1% (m/m) of 950 K molecular weight PMMA in anisole solvent) was used as described in the original protocol.[56] The PMMA was overlaid with 100 nm of amorphous silicon (a-Si) followed by the deposited DNA origami and the patterned silicon oxide masking layer (10–20 nm). The layers were then sequentially etched with RIE and metal was deposited on the chips with electron-beam PVD. The processing was completed by removing the PMMA, a-Si and $SiO_2$ films by dissolving the underlying PMMA.[56]

The end product is the initial glass substrate, which is covered with origami-shaped, but significally rounded, silver patterns. These nanostructures consist of a 2 nm thick layer of Ti (an adhesive layer) and a subsequently deposited 20 nm layer of Ag. The areal coverage of both samples were approximately equal (~1%), implying that the possible differences in optical properties are governed by the shapes and sizes of the particles. The details of determining particle coverage and large-scale images of the patterned surfaces are presented in the ESI (Fig. S2–S7†).

Fabricated structures (Fig. 1b) were analyzed with scanning electron microscopy using a Zeiss Sigma VP SEM with a Schottky field emission gun at a 10 kV acceleration voltage. An in-lens detector was used for viewing the structures.

Following the BLIN processing and imaging, all samples (bowtie and single triangle structures) were spincoated with a PMMA A1 layer of roughly 40 nm thickness to prevent further oxidation and abrasion.

### 2.3. Transmission and Raman measurement

Prior to measurements, the PMMA layer was removed by inserting the samples into an acetone (Honeywell, VLSI, ≥99.5%) solution followed by heating the mixture close to boiling point (52 °C) for ~10 minutes. Samples were subsequently cleaned in isopropanol (IPA) (Honeywell, VLSI, ≥99.8%) solution to remove any PMMA residues and finally blow dried with nitrogen gas. Then a solution of R6G was prepared by dissolving 5 mg of R6G into 4 ml of PMMA A3. Finally, the R6G solution was spincoated on the structures at 3000 rpm for 30 s producing a R6G layer of ~120 nm thickness.

Optical measurements were conducted to determine the transmission properties of the structures (single triangles and bowties). The experimental setup (Fig. 1c) and the procedures are explained in detail elsewhere.[58] A commercial Renishaw InVia Reflex Raman microscope was used to measure Raman signals of R6G on both samples using a laser excitation wavelength of 785 nm.

### 2.4. FDTD simulations

The numerical calculations for the bowtie and triangle nanoparticles were performed using polarization resolved simulations (Lumerical FDTD Solutions). In these simulations, the boundary conditions were set to the perfectly matched layer (PML), and total-field scattered-field (TFSF) was chosen as the light source to better characterize the scattering spectrum of small particles illuminated with a plane wave. PML as an artificial absorption layer can fully absorb light scattered by the particle without reflection back to the particle. The TFSF source, meanwhile, uses plane wave excitation and is commonly used together with PML boundary conditions when solving absorption or scattering problems. The TFSF source allows one to obtain the absorption and scattering as well as their sum, namely the extinction cross-section. The simulated absorption and scattering spectra for a single triangle and a bowtie are presented in ESI Fig. S8 and S9.† Both bowtie and triangle nanoparticles were 20 nm in height and they were placed onto a $SiO_2$ substrate overlaid with a 17 nm thick ITO layer. The bowtie gap size was set to 10 nm. The particle material parameters for Ag used for simulations were adopted from the CRC handbook[59] to match the fabrication method mentioned above.

 

## 3. Results

Fig. 2 illustrates the extinction (experimental and simulation) spectra for both single triangles and bowties. Fig. 2a and b correspond to the experimental results of ensemble averaged extinction ratios while Fig. 2c and d show the simulated extinction spectra for an individual triangle and bowtie. The experimental extinction spectra of the single triangles show approximately constant extinction ratio of 5–10% in the studied wavelength range. Meanwhile, the bowtie structures display two resonances at peak wavelengths of ~700 nm and ~890 nm, with extinction ratios of ~18% and ~23%, respectively.

Since the nanoparticles adopt random orientations on the substrate, the polarization resolved analysis is not experimentally feasible. For polarization specific analysis, we present the corresponding simulation results at different polarization directions. For single triangles, experimental and simulated spectra are somewhat featureless in the studied wavelength regime except for the simulated excitation peak at around 900 nm. The simulations of bowtie structures exhibit various resonances depending on the polarization. The transverse polarization exhibits a peak at 650 nm, whereas the longitudinal polarization has two peaks at 700 nm and at 850 nm.

Due to random orientations of the structures obtained by BLIN, the polarization averaged extinction cross-section (black curve in Fig. 2c and d) gives the most realistic comparison with the experimentally obtained spectra. Altogether, the experimentally determined excitation peaks of bowties (Fig. 2b) match well with the simulated ones of an individual bowtie structure (Fig. 2d). The higher extinction ratio of bowtie ensembles (Fig. 2b) compared to single triangles (Fig. 2a) can be associated either with their higher number density (same areal coverage of bowties and single triangles corresponds to higher number density of bowties) or with optical resonances.

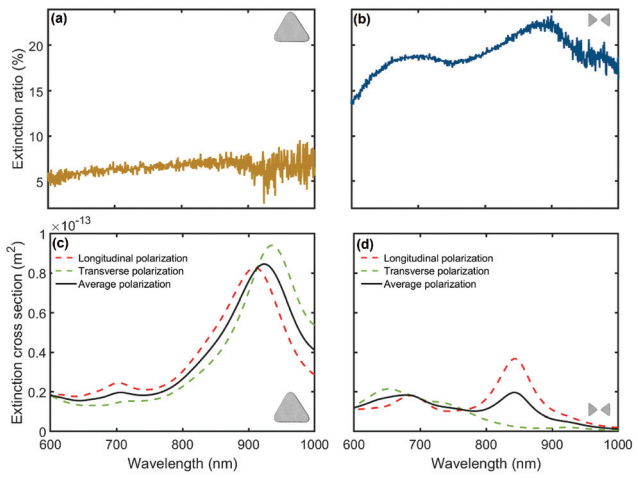


**Fig. 2** Experimentally obtained extinction spectra ($1 - T$) as a function of wavelength for (a) single triangles and (b) bowties. (c and d) The corresponding simulations of the far-field distributions, which show extinction cross-sections ($m^2$) *vs.* wavelength at different polarization directions. Red dotted line: longitudinal polarization, green dotted line: transverse polarization, continuous black line: average polarization.

To study the optical resonances in detail, simulations of the near-field distributions for a single triangle and a bowtie (Fig. 3a and b) were performed. The electric field enhancement profiles are presented at four different wavelengths, namely, Raman excitation wavelength (785 nm) and at the Raman transition wavelengths of R6G (873 nm, 877 nm, and 890 nm). The single triangles (Fig. 3a) show moderate field enhancements ranging from 4 to 10 for both polarizations. Interestingly, for the longitudinal polarization, bowtie structures (Fig. 3b, top panel) exhibit higher enhancements than the single triangles in the gap region. At the Raman transition wavelengths of R6G the field enhancements reach values of ~20. Thus, the ability to fabricate nanoscale structures in a parallel fashion and to produce nanoscale gaps for maximal field enhancement demonstrates the application potential of the presented BLIN method.

Next, we present the potential of BLIN structures for surface-enhanced Raman scattering (SERS). The experimentally obtained Raman spectra of both single large triangles and bowties are presented in Fig. 4. We observe three clear Raman peaks[58] related to R6G molecules, namely at 1290 $cm^{-1}$, 1345 $cm^{-1}$, and 1490 $cm^{-1}$, and one less pronounced peak at 1650 $cm^{-1}$. Single triangles appear to exhibit

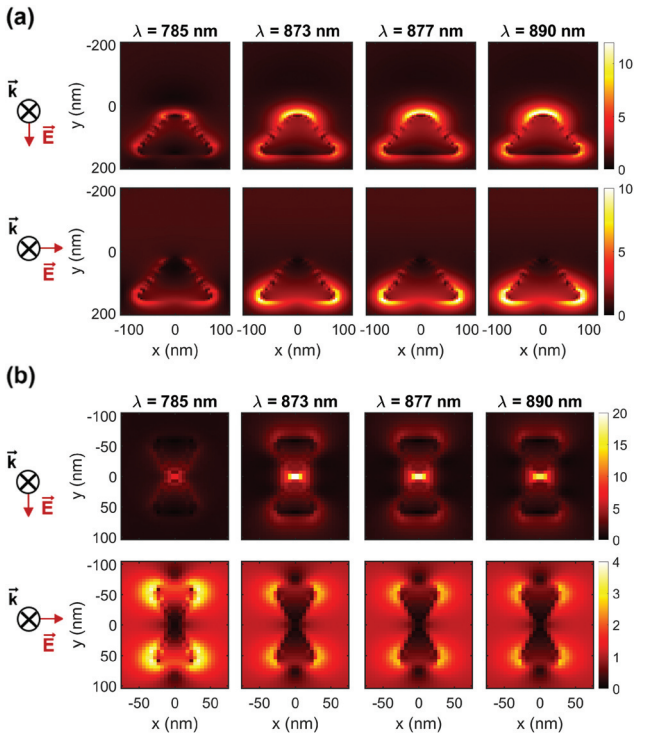


**Fig. 3** Simulations showing near-field distributions of (a) a single Ag triangle (b) a bowtie-shaped structure with a gap size of 10 nm. The electric field enhancement profiles are presented at the Raman excitation wavelength (785 nm) and at the Raman transition wavelengths of Rhodamine 6G (873 nm, 877 nm, and 890 nm) for both polarizations. The upper panels in both (a) and (b) represent electric field enhancement profiles for longitudinal polarization, while the bottom panels correspond to that of transverse polarization.

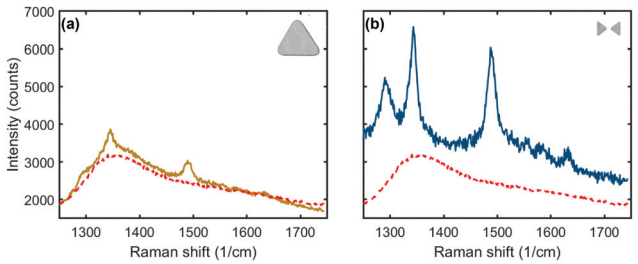


**Fig. 4** Raman spectra of Rhodamine 6G coated substrates showing Raman intensities as a function of Raman shift for (a) single triangles and (b) bowties. Raman spectrum of the R6G on a bare substrate is presented in both plots as a red dotted curve. R6G molecules exhibit Raman peaks at 1345 $cm^{-1}$ and 1490 $cm^{-1}$ for both single triangles and bowties structures. Additional R6G Raman peaks in the case of bowtie are observed at 1290 $cm^{-1}$ and 1650 $cm^{-1}$. The equivalencies of these Raman peaks are at wavelengths 873 nm, 877 nm, 890 nm and 902 nm (in ascending order).

only a weak R6G Raman signal with two distinguishable peaks at 1345 $cm^{-1}$ and 1490 $cm^{-1}$ (Fig. 4a). In contrast, for the bowtie samples three very pronounced R6G Raman peaks at 1290 $cm^{-1}$, 1345 $cm^{-1}$, 1490 $cm^{-1}$, and one less pronounced peak at 1650 $cm^{-1}$, can be identified as depicted in Fig. 4b. Overall, the intensity of each individual Raman peak of the bowtie sample is about four times that of the single triangle. As the areal coverage of the single triangles and bowties are equal, the higher SERS enhancements of bowties can be associated with the BLIN-enabled nanoscale patterning. Further, the simulations indicate an intimate connection between the nanoscopic gaps and the field enhancements. As conventional electron beam lithography unavoidably suffers from proximity effects related to electron scattering, BLIN provides an intriguing alternative for fabricating nanoscale structures, and in particular nanoscale gaps. The parallel nature of the fabrication can allow for affordable, high throughput fabrication of various functional substrates, for instance for SERS as demonstrated here.

## 4. Conclusions

To conclude, we have optically characterized BLIN-fabricated nanostructures and shown that they are optically resonant. Single triangles and bowtie-shaped structures with narrow nanoscale gaps were fabricated and characterized optically. We have shown that the equal areal coverage of the single triangles and bowties results in a significantly enhanced SERS signal for the bowties. This enhancement and the obtained extinction spectra of the samples are supported by the FDTD simulated data. Thus, the ability to fabricate not only nanoscopic structures, but also nanoscale gaps with our technique makes it particularly appealing to applications, where plasmonic hotspots are needed. We believe that with further optimization, it is possible to achieve sub-10 nm gaps by controlling the silicon oxide growth, similarly as with previously published protocols.[54,60]

The current possibilities to knock down the price of DNA origami synthesis,[61] deposit DNA nanostructures at large scales[62] and build hierarchical ordered DNA assemblies covering up to ~10 $cm^2$ areas[63] pave the way for self-assembly-based up-scaled substrate manufacturing. The results presented here could open up avenues for customizable optically resonant surface fabrication, as the DNA origami platform enables adjustment of shape, density, chirality and gap/feature sizes of the patterned units[54] for adapting to analyte-/application-specific purposes. Besides the demonstrated intriguing optical properties of single DNA origami-shaped nanoparticles and their subsequent prospects arising from the manipulation of the resonance wavelengths and the adjustable field enhancements,[64] the combination of programmable lattice-forming DNA units and the BLIN technique may further yield highly ordered nanopatterns with collective metasurface-enabled effects.[65,66]

## Conflicts of interest

There are no conflicts to declare.

## Acknowledgements

This work is part of the Academy of Finland Flagship Programme, Photonics Research and Innovation (PREIN), decision 321066. Financial support from Academy of Finland (project numbers 322002, 322022 and 324353), Emil Aaltonen Foundation, Jane and Aatos Erkko Foundation, Sigrid Jusélius Foundation, Magnus Ehrnrooth Foundation, Finnish Cultural Foundation (Kalle and Dagmar Välimaa Fund) and Vilho, Yrjö and Kalle Väisälä Foundation of the Finnish Academy of Science and Letters is gratefully acknowledged. This work was carried out under the Academy of Finland Centers of Excellence Program (2022–2029) in Life-Inspired Hybrid Materials (LIBER), project number (346110). We acknowledge the provision of facilities and technical support by Aalto University Bioeconomy Facilities and OtaNano – Nanomicroscopy Center (Aalto-NMC) and Micronova Nanofabrication Center.

## References

1 C.-H. Chou and F.-C. Chen, *Nanoscale*, 2014, **6**, 8444–8458.
2 W. Ye, R. Long, H. Huang and Y. Xiong, *J. Mater. Chem. C*, 2017, **5**, 1008–1021.
3 J. Mejía-Salazar and O. N. Oliveira Jr., *Chem. Rev.*, 2018, **118**, 10617–10625.
4 Y. Li, C. Jing, L. Zhang and Y.-T. Long, *Chem. Soc. Rev.*, 2012, **41**, 632–642.
5 G. J. Leggett, *ACS Nano*, 2011, **5**, 1575–1579.

6 R. Liu, Q. Wu, Y. Shan, Z. Wang, T. Zheng and K. Li, *Integr. Ferroelectr.*, 2017, **182**, 90–97.
7 N. C. Seeman, *J. Theor. Biol.*, 1982, **99**, 237–247.
8 S. Nummelin, J. Kommeri, M. A. Kostiainen and V. Linko, *Adv. Mater.*, 2018, **30**, 1703721.
9 N. C. Seeman and H. F. Sleiman, *Nat. Rev. Mater.*, 2018, **3**, 17068.
10 S. Surana, A. R. Shenoy and Y. Krishnan, *Nat. Nanotechnol.*, 2015, **10**, 741–747.
11 A. Keller and V. Linko, *Angew. Chem., Int. Ed.*, 2020, **59**, 15818–15833.
12 P. Piskunen, R. Latham, C. E. West, M. Castronovo and V. Linko, *iScience*, 2022, **25**, 104389.
13 L. Hui, R. Bai and H. Liu, *Adv. Funct. Mater.*, 2022, **32**, 2112331.
14 M. DeLuca, Z. Shi, C. E. Castro and G. Arya, *Nanoscale Horiz.*, 2020, **5**, 182–201.
15 S. Nummelin, B. Shen, P. Piskunen, Q. Liu, M. A. Kostiainen and V. Linko, *ACS Synth. Biol.*, 2020, **9**, 1923–1940.
16 M. Pilo-Pais, G. P. Acuna, P. Tinnefeld and T. Liedl, *MRS Bull.*, 2017, **42**, 936–942.
17 A. Heuer-Jungemann and V. Linko, *ACS Cent. Sci.*, 2021, **7**, 1969–1979.
18 P. W. K. Rothemund, *Nature*, 2006, **440**, 297–302.
19 S. M. Douglas, H. Dietz, T. Liedl, B. Högberg, F. Graf and W. M. Shih, *Nature*, 2009, **459**, 414–418.
20 V. Linko and M. A. Kostiainen, *Nat. Biotechnol.*, 2016, **34**, 826–827.
21 S. Dey, C. Fan, K. V. Gothelf, J. Li, C. Lin, L. Liu, N. Liu, M. A. D. Nijenhuis, B. Saccà, F. C. Simmel, H. Yan and P. Zhan, *Nat. Rev. Methods Primers*, 2021, **1**, 13.
22 Z.-G. Wang, Q. Liu and B. Ding, *Chem. Mater.*, 2014, **26**, 3364–3367.
23 J. B. Knudsen, L. Liu, A. L. B. Kodak, M. Madsen, Q. Li, J. Song, J. B. Woehrstein, S. F. J. Wickham, M. T. Strauss, F. Schueder, J. Vinther, A. Krissanaprasit, D. Gudnason, A. A. A. Smith, R. Ogaki, A. N. Zelikin, F. Besenbacher, V. Birkedal, P. Yin, W. M. Shih, R. Jungmann, M. Dong and K. V. Gothelf, *Nat. Nanotechnol.*, 2015, **10**, 892–898.
24 H. T. Maune, S.-p. Han, R. D. Barish, M. Bockrath, W. A. Goddard III, P. W. K. Rothemund and E. Winfree, *Nat. Nanotechnol.*, 2010, **5**, 61–66.
25 M. Zhao, Y. Chen, K. Wang, Z. Zhang, J. K. Streit, J. A. Fagan, J. Tang, M. Zheng, C. Yang, Z. Zhu and W. Sun, *Science*, 2020, **368**, 878–881.
26 E. Graugnard, W. L. Hughes, R. Jungmann, M. A. Kostiainen and V. Linko, *MRS Bull.*, 2017, **42**, 951–959.
27 M. Scheckenbach, J. Bauer, J. Zähringer, F. Selbach and P. Tinnefeld, *APL Mater.*, 2020, **8**, 110902.
28 A. Kuzyk, R. Schreiber, Z. Fan, G. Pardatscher, E.-M. Roller, A. Högele, F. C. Simmel, A. O. Govorov and T. Liedl, *Nature*, 2012, **483**, 311–314.
29 A. Kuzyk, R. Schreiber, H. Zhang, A. O. Govorov, T. Liedl and N. Liu, *Nat. Mater.*, 2014, **13**, 862–866.
30 V. V. Thacker, L. O. Herrmann, D. O. Sigle, T. Zhang, T. Liedl, J. J. Baumberg and U. F. Keyser, *Nat. Commun.*, 2014, **5**, 3448.
31 E.-M. Roller, L. V. Besteiro, C. Pupp, L. K. Khorashad, A. O. Govorov and T. Liedl, *Nat. Phys.*, 2017, **13**, 761–765.
32 P. Zhan, T. Wen, Z.-g. Wang, Y. He, J. Shi, T. Wang, X. Liu, G. Lu and B. Ding, *Angew. Chem., Int. Ed.*, 2018, **57**, 2846–2850.
33 B. Shen, M. A. Kostiainen and V. Linko, *Langmuir*, 2018, **34**, 14911–14920.
34 M. Pfeiffer, K. Trofymchuk, S. Ranallo, F. Ricci, F. Steiner, F. Cole, V. Glembockyte and P. Tinnefeld, *iScience*, 2021, **24**, 103072.
35 T. Zhang, C. Hartl, K. Frank, A. Heuer-Jungemann, S. Fischer, P. C. Nickels, B. Nickel and T. Liedl, *Adv. Mater.*, 2018, **30**, 1800273.
36 S. Julin, A. Korpi, B. Shen, V. Liljeström, O. Ikkala, A. Keller, V. Linko and M. A. Kostiainen, *Nanoscale*, 2019, **11**, 4546–4551.
37 Y. Tian, J. R. Lhermitte, L. Bai, T. Vo, H. L. Xin, H. Li, R. Li, M. Fukuto, K. G. Yager, J. S. Kahn, Y. Xiong, B. Minevich, S. K. Kumar and O. Gang, *Nat. Mater.*, 2020, **19**, 789–796.
38 V. Linko and M. A. Kostiainen, *Nat. Mater.*, 2020, **19**, 706–707.
39 G. Zhang, S. P. Surwade, F. Zhou and H. Liu, *Chem. Soc. Rev.*, 2013, **42**, 2488–2496.
40 R. Wang, G. Zhang and H. Liu, *Curr. Opin. Colloid Interface Sci.*, 2018, **38**, 88–99.
41 F. Liu, Y. Shang, Z. Wang, Y. Jiao, N. Li and B. Ding, *APL Mater.*, 2020, **8**, 110703.
42 I. V. Martynenko, V. Ruider, M. Dass, T. Liedl and P. C. Nickels, *ACS Nano*, 2021, **15**, 10769–10774.
43 C. Vietz, M. L. Schütte, Q. Wei, L. Richter, B. Lalkens, A. Ozcan, P. Tinnefeld and G. P. Acuna, *ACS Omega*, 2019, **4**, 637–642.
44 K. Trofymchuk, V. Glembockyte, L. Grabenhorst, F. Steiner, C. Vietz, C. Close, M. Pfeiffer, L. Richter, M. L. Schütte, F. Selbach, R. Yaadav, J. Zähringer, Q. Wei, A. Ozcan, B. Lalkens, G. P. Acuna and P. Tinnefeld, *Nat. Commun.*, 2021, **12**, 950.
45 A. T. M. Yeşilyurt and J.-S. Huang, *Adv. Opt. Mater.*, 2021, **9**, 2100848.
46 S. Helmi, C. Ziegler, D. J. Kauert and R. Seidel, *Nano Lett.*, 2014, **14**, 6693–6698.
47 W. Sun, E. Boulais, Y. Hakobyan, W. L. Wang, A. Guan, M. Bathe and P. Yin, *Science*, 2014, **346**, 1258361.
48 J. Ye, O. Aftenieva, T. Bayrak, A. Jain, T. A. F. König, A. Erbe and R. Seidel, *Adv. Mater.*, 2021, **33**, 2100381.
49 A. Gopinath and P. W. K. Rothemund, *ACS Nano*, 2014, **8**, 12030–12040.
50 R. M. Shetty, S. R. Brady, P. W. K. Rothemund, R. F. Hariadi and A. Gopinath, *ACS Nano*, 2021, **15**, 11441–11450.
51 A. Gopinath, E. Miyazono, A. Faraon and P. W. K. Rothemund, *Nature*, 2016, **535**, 401–405.

52 A. Gopinath, C. Thachuk, A. Mitskovets, H. A. Atwater, D. Kirkpatrick and P. W. K. Rothemund, *Science*, 2021, **371**, eabd6179.
53 B. Shen, V. Linko, K. Tapio, M. A. Kostiainen and J. J. Toppari, *Nanoscale*, 2015, **7**, 11267–11272.
54 B. Shen, V. Linko, K. Tapio, S. Pikker, T. Lemma, A. Gopinath, K. V. Gothelf, M. A. Kostiainen and J. J. Toppari, *Sci. Adv.*, 2018, **4**, eaap8978.
55 P. Piskunen, B. Shen, S. Julin, H. Ijäs, J. J. Toppari, M. A. Kostiainen and V. Linko, *J. Vis. Exp.*, 2019, **151**, e60313.
56 P. Piskunen, B. Shen, A. Keller, J. J. Toppari, M. A. Kostiainen and V. Linko, *ACS Appl. Nano Mater.*, 2021, **4**, 529–538.
57 S. P. Surwade, F. Zhou, B. Wei, W. Sun, A. Powell, C. O'Donnell, P. Yin and H. Liu, *J. Am. Chem. Soc.*, 2013, **135**, 6778–6781.
58 K. Alam, K. M. Kabusure, B. O. Asamoah, T. Nuutinen, M. Baah, S. Mohamed, A. Matikainen, J. Heikkinen, H. Rekola, M. Roussey, M. Kuittinen and T. K. Hakala, *Nanoscale*, 2020, **12**, 23166–23172.
59 *CRC Handbook of Chemistry and Physics*, CRC Press, 95th edn, 2014.
60 B. Shen, V. Linko and J. J. Toppari, DNA-Assisted Molecular Lithography, In *DNA Nanotechnology. Methods in Molecular Biology*, Humana Press, New York, NY, 2018, vol. 1811, pp. 299–314.
61 F. Praetorius, B. Kick, K. L. Behler, M. N. Honemann, D. Weuster-Botz and H. Dietz, *Nature*, 2017, **552**, 84–87.
62 V. Linko, B. Shen, K. Tapio, J. J. Toppari, M. A. Kostiainen and S. Tuukkanen, *Sci. Rep.*, 2015, **5**, 15634.
63 Y. Xin, B. Shen, M. A. Kostiainen, G. Grundmeier, M. Castro, V. Linko and A. Keller, *Chem. – Eur. J.*, 2021, **27**, 8564–8571.
64 A. Sundaramurthy, K. B. Crozier, G. S. Kino, D. P. Fromm, P. J. Schuck and W. E. Moerner, *Phys. Rev. B: Condens. Matter Mater. Phys.*, 2005, **72**, 165409.
65 V. Shalaev, *Nat. Photonics*, 2007, **1**, 41–48.
66 N. Yu and F. Capasso, *Nat. Mater.*, 2014, **13**, 139–150.